



Killing Two Birds with One Stone: A Highly Active Tubular Carbon Catalyst with Effective N Doping for Oxygen Reduction and Hydrogen Evolution Reactions

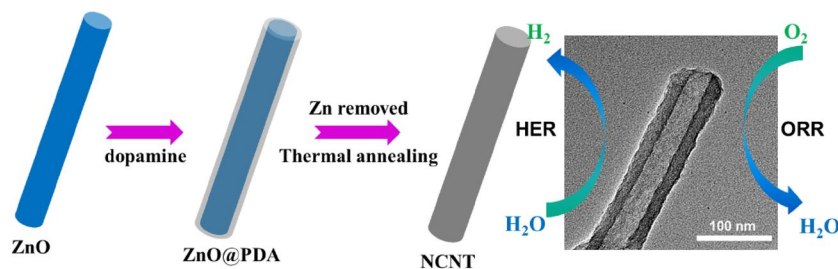
Yanqiang Li¹ · Huiyong Huang¹ · Siru Chen³ · Chao Wang¹ · Anmin Liu¹ · Tingli Ma²

Received: 20 September 2018 / Accepted: 6 December 2018 / Published online: 17 December 2018
© Springer Science+Business Media, LLC, part of Springer Nature 2018

Abstract

The oxygen reduction reaction (ORR) and hydrogen evolution reaction (HER) are two of the core reactions that occur in fuel cells and water electrolysis devices. Heteroatom-doped carbon materials are promising metal-free electrocatalysts to improve the conversion efficiency of these devices. To optimize the nanostructures of such carbon-based catalysts, herein, we reported an effective template method to synthesize N doped carbon nanotubes by using polydopamine as a precursor. The use of the ZnO nanowire not only serves as a self-sacrificial template to direct the formation of the nanotube, but also greatly extends the porosity of the carbon nanotube. Moreover, the polydopamine precursor also leads to effective N doping. An optimized sample, NCNT-900, shows high ORR performance comparable with that of Pt/C as well as good HER performance in both alkaline and acid media, making it one of the most effective carbon-based HER catalysts. This strategy offers an opportunity to synthesize catalysts with higher activity by rational design of a carbon precursor with higher N content or multi-heteroatom co-doping.

Graphical Abstract



Nitrogen doped carbon nanotube with high performance for both ORR and HER was synthesized using ZnO nanowires as template. The obtained materials show effective N doping that provides abundant active sites, high surface area and unique textural parameters that can effectively enhance mass transfer. When used for electrocatalysts, NCNT-900 shows high ORR performance comparable with that of Pt/C and good HER performance in both alkaline and acid media.

Keywords Electrocatalysis · Oxygen reduction reaction · Hydrogen evolution reaction · Metal-free catalysts · Carbon nanotubes

Electronic supplementary material The online version of this article (<https://doi.org/10.1007/s10562-018-2636-5>) contains supplementary material, which is available to authorized users.

Extended author information available on the last page of the article

1 Introduction

Sustainable clean energy storage and conversion devices, such as fuel cells, metal-air batteries and water splitting devices have attracted great attention due to ever-increasing global energy consumption and environmental pollution [1–3]. Clean energy technology is closely related to several

important reactions including the hydrogen evolution reaction (HER), oxygen reduction reaction (ORR) and oxygen evolution reaction (OER) [4–6]. In fuel cells, the sluggish ORR kinetics at the cathode is a major limitation as the anodic hydrogen oxidation reaction is orders of magnitude faster [7]. Moreover, it is also very important to produce hydrogen effectively from water as O_2 can arise from air. To date, the most effective catalysts toward ORR and HER are platinum-based catalysts [8–10]. However, the scarcity and high cost of Pt, as well as poor long-term stability limits their widespread application. Actually, most metal-based catalysts face the durability issue due to aggregation that occurs during operation [11, 12]. In comparison, metal-free carbon-based catalysts usually show better durability and can be used as potential electrocatalysts, even though the catalytic activities of carbons are not sufficiently high [13–15].

Recently, it has been reported that the catalytic activity of carbon-based catalysts can be improved through heteroatoms doping [16, 17]. Both theory and experiment reveal that heteroatom doping can be used to activate carbon's π electrons and create extra catalytic active sites [18, 19]. Moreover, multi heteroatoms co-doping can further enhance the catalytic activity of carbon due to the synergistic effect of different heteroatoms [20–22]. For example, Qiao et. al. investigated the HER activity of nitrogen-doped carbon nanosheets with secondary heteroatoms, and found that S atoms have a better promotional effect than P and B [23]. By introducing S atoms into MOF-derived N doped carbon, Sun et. al. demonstrated that the synergistic effect of N and S co-doping can create active sites with higher catalytic activity for ORR than isolated N and S-dopants [24]. However, it should be noted that introducing extra doping sources can inevitably complicate the preparation process and compromise the experimental repeatability. Thus, it is highly desirable to develop new strategies to improve the catalytic activity of single heteroatom doped carbon.

In addition to heteroatom doping, the optimization of a catalyst's macrostructure is also an effective method to improve catalytic activity, as the catalytic performance not only relies on the active sites of the catalysts, but also on the mass and charge transfer across the electrode–electrolyte interface. Jiang's group has reported that a high surface area and multicomponent active dopants are both essential for improving catalytic performance [25]. Ferrero's research also revealed that a bimodal mesoporous structure can act as interconnected highways to provide rapid and full transport towards/from the catalytic sites for both reactant and products, highlighting the importance of pore size distribution [26]. Moreover, the effective bonding configuration of the heteroatoms is also very important as the pyridine-like N and graphite-like N (also named quaternary N) are more active than pyrrole-type N [27–29]. Therefore, an optimized

structure with effective active sites should result in optimum electrocatalytic performance.

Herein, we report a novel method for the synthesis of N doped carbon nanotube (NCNT) by using ZnO nanowires as a template, polydopamine (PDA) as C and N sources. Through in situ polymerization of dopamine on the ZnO wire, ZnO@PDA nanowires can be facilely synthesized. Further thermal annealing the ZnO@PDA in N_2 enables one to remove the ZnO template and obtain the NCNT. Moreover, the evaporation of Zn during thermal annealing can create sufficient voids on the NCNT, leading to a high surface area. In addition, the NCNTs show up to 70–80% graphite-like and pyridine-like N, making it very effective as an electrocatalyst for ORR and HER. The optimized catalyst NCNT-1000 shows ORR performance that is comparable with commercial Pt/C catalysts in alkaline media as well as excellent durability and tolerance for methanol. Moreover, the HER performance of NCNT-1000 is also comparable with those of metal-free carbon-based catalysts reported previously. Together with the sustainable green approach, the NCNT electrocatalysts show great potential for application in proton exchange membrane fuel cells and water splitting devices.

2 Experimental Section

2.1 Preparation of One-Dimensional ZnO@PDA and NCNTs

First, uniform ZnO nanowires were prepared according to a previous report [30]. Then the ZnO nanowires were used as a template to prepare the NCNTs. To prepare ZnO@PDA nanowires, 100 mg of ZnO nanowires were dispersed in solution mixtures of deionized water (20 mL) and ethanol (20 mL). Then dopamine (250 mg) in Tris–HCl (pH = 8.5, 40 mL, 50 mM) was added. The solution was stirred at room temperature for 12 h to polymerize the dopamine. Then the solid was collected by centrifugation to obtain ZnO@PDA. The ZnO@PDA was then thermal annealed at different temperatures under N_2 for 1 h to prepare the carbon nanotubes. The obtained samples were denoted as NCNT-x, where x is the thermal annealing temperature.

2.2 Characterization

Powder X-ray diffraction (PXRD) patterns were collected using a Rigaku D/MAX2550 diffractometer. Raman spectra measurements were conducted using a Renishaw inVia Raman spectrometer equipped with an Ar ion laser operating at a wavelength of 514.5 nm. The structure and morphology of the catalysts were characterized using a field Emission Scanning Electron Microscope (FEI, Nova NanoSEM 450)

and field-emission TEM (FEI, Tecnai G2 F30). X-ray photoelectron spectroscopy (XPS) measurement were conducted using an ESCALAB 250Xi (ThermoFisher) to analyze the surface states of chemical elements, with the binding energy of the C 1s peak at 284.8 eV used as an internal reference. Nitrogen adsorption/desorption measurements were carried out using an Autosorb-iQ2 (Quantachrome Instruments) at 77 K to determine the surface areas and pore size distributions. The specific surface areas were calculated using nitrogen adsorption data by multipoint BET analysis. Pore size distributions were analyzed using the N_2 adsorption data according to quenched solid density functional theory (QSDFT, nitrogen on carbon, slit pore).

2.3 Electrochemical Measurements

The catalytic measurements were carried out using a standard three-electrode system with a rotating disk electrode (RDE) device (Pine Instrument Company) connected to a CHI 660C potentiostat workstation. A Pt wire was used as a counter electrode and Ag/AgCl was used as a reference electrode. The working electrode was a glassy carbon disk with a diameter of 5 mm.

For the preparation of the working electrode, the electroactive material (2 mg) was ultrasonically dispersed in a water (480 μ L) and isopropanol (480 μ L) mixture containing 20 μ L of 5 wt% Nafion® solution until a homogeneous catalyst ink was obtained. Thereafter, 15 μ L of the above dispersion was drop-cast onto the glassy carbon electrode to obtain a catalyst loading of ~ 0.16 mg cm^{-2} . Pt/C (20 wt%, Alfa Aesar) catalyst ink was prepared according to the same procedure for comparison.

For the ORR test, 0.1 M KOH was used as the electrolyte, which was bubbled with O_2 for 30 min to reach oxygen saturation before measurement. The kinetics parameters during ORR were determined according to the Koutecky–Levich equations:

$$1/j = 1/j_k + 1/(B\omega^{1/2})$$

$$B = 0.2nFC_0(D_0)^{2/3}\nu^{-1/6}$$

where j is measured current, j_k is the kinetic current, ω is the electrode rotation rate in rpm, n is the number of electrons transferred per mole of O_2 . The constant 0.2 is feasible when the rotation rate is in rpm, F is the Faraday constant (96,485 C mol^{-1}), D_0 is the diffusion coefficient of O_2 in (1.9×10^{-5} $cm^2 s^{-1}$), C_0 is the bulk concentration of O_2 (1.2×10^{-3} mol L^{-1}) and ν is the kinetic viscosity (0.01 $cm^2 s^{-1}$) of 0.1 M KOH.

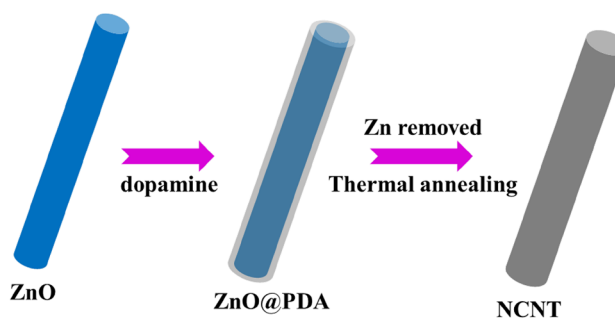
For HER test, the electrolyte was 1.0 M KOH or 0.5 M H_2SO_4 , which was bubbled with N_2 for 30 min before measurement. Cyclic voltammograms (CV) were recorded under similar conditions and at different scan rates (20–200 $mV s^{-1}$) between 0.3 and 0.6 V to evaluate the electrochemical double layer capacitance (C_{dl}), representing the electrochemically active surface area (ESCA).

All potentials were measured against the reference electrode and converted to the reversible hydrogen electrode (RHE) reference scale by formula $E(RHE) = E(Ag/AgCl) + 0.059 pH + 0.197$. The current densities in both the CV and RDE data were normalized to the geometric area (0.196 cm^2) of the glassy carbon electrode.

3 Results and Discussions

3.1 Structure Characterization

A schematic illustration for the preparation of the NCNTs is shown in Scheme 1. The usage of ZnO as a template has unique advantages. First, abundant oxygen-containing species on the surface of ZnO enable uniform polymerization of the dopamine on it. Second, when thermally annealed at high temperatures, the polydopamine can be carbonized into carbon, with ZnO easily reduced to Zn by the carbon at high temperature. Last and most significantly, the low boiling point of Zn (908 $^{\circ}C$) means that it can be evaporated at high temperature such as 900 $^{\circ}C$. During its evaporation, the Zn vapor will pass across the carbon and create many voids, leading to porous carbon with a high surface area. Moreover, this method can simplify the preparation procedure, as no extra washing process is needed to remove the template. For example, silica can also be used as template to synthesis porous materials; however, extensive post-washing using HF or NaOH was needed to remove the silica template [31, 32]. Scanning electron microscopy (SEM) images are collected to monitor the formation of the NCNT. First, uniform ZnO nanowires with lengths in the range of 2–4 μ m and widths



Scheme 1 Schematic illustration of the synthetic procedure used for the preparation of the NCNTs

of 100 nm are prepared and used as a template (Figure S1). Then, dopamine was in situ polymerized onto the surface of ZnO nanowires in a Tris–HCl solution at room temperature to form ZnO@PDA. The polymerization process of dopamine does not affect the morphology as this occurs near neutral conditions (pH = 8.5) (Fig. 1a). The thermal annealing temperature has a great influence on the formation of the NCNT. As shown in Figure S2, when the temperature is 800 °C, a significant amount of ZnO remains in the obtained product due to the temperature being far below the boiling point of ZnO, with HCl washing needed to remove the ZnO. By weighting the mass of the sample before and after HCl washing, it is found that 27 wt% ZnO remains in the sample after thermal annealing at 800 °C. When the temperature is increased to 900 °C and 1000 °C, the Zn species can be removed completely and a pure carbon nanotube obtained. From the SEM images in Fig. 1, it can be seen that all the catalysts show well-defined tubular structures with a similar diameter and length. TEMs images also demonstrated the formation of a tubular structure (Fig. 1e and Figure S3). From the high resolution TEM image, abundant pores can be observed, indicating that the carbon nanotube may possess a very high surface area (Fig. 1f). From the elemental mapping images in Fig. 1g, we can see that C, N, and O are distributed homogeneously in the overall carbon nanotube, demonstrating that the N atoms in dopamine are doped into the carbon nanotube. Moreover, Zn elemental mapping is also shown in Figure S4. It can be seen that only a few scattered distributions exist other than dense nanotube shape composed of C, N and O, indicating that the Zn element is completely evaporated.

The structure and composition of the carbons were first examined by powder XRD. As shown in Fig. 2a, all the samples exhibit an obvious peak at 24°, which can be attributed to the (002) plane of carbon, demonstrating that the polydopamine was carbonized into carbon [33]. In addition, the carbons are mainly amorphous as the diffraction peak is not very sharp. Raman spectroscopy also demonstrated successful formation of the carbon structure (Fig. 2b). The two obvious peaks located at 1360 and 1580 cm^{-1} can be ascribed to the D and G band of graphite, with all the catalysts showing a similar I_G/I_D value, indicating that the catalysts possess a similar degree of graphitization. X-ray photoelectron spectroscopy (XPS) was used to examine the elemental composition and chemical bonding of the carbon catalysts. From the survey spectra shown in Figure S5, we can observe three obvious peaks centered at 285, 400 and 532 eV, corresponding to the C 1s, N 1s and O 1s peaks. No peak at 1020 eV (the Zn element peak) is observed, indicating that the Zn species were completely removed by high temperature or acid washing. The high-resolution C 1s spectra can be divided into three peaks at 284.6, 285.7 and 286.5 eV, which can be ascribed to trigonal bonded carbon (sp^2 centers), tetrahedral bonded carbon (sp^3 centers) and C–O and C–N groups, respectively (Fig. 2c) [34, 35]. Moreover, the C element accounts for more than 90% of the catalysts, indicating that the catalysts are composed mostly of carbon (Table S1). From Table S1, we can also see that with increasing temperature, the N content is decreased due to its unstable character at high temperature. The high-resolution nitrogen 1s spectrum can be split into four peaks, corresponding to pyridinic N (398.5 eV), pyrrolic N (399.6 eV),

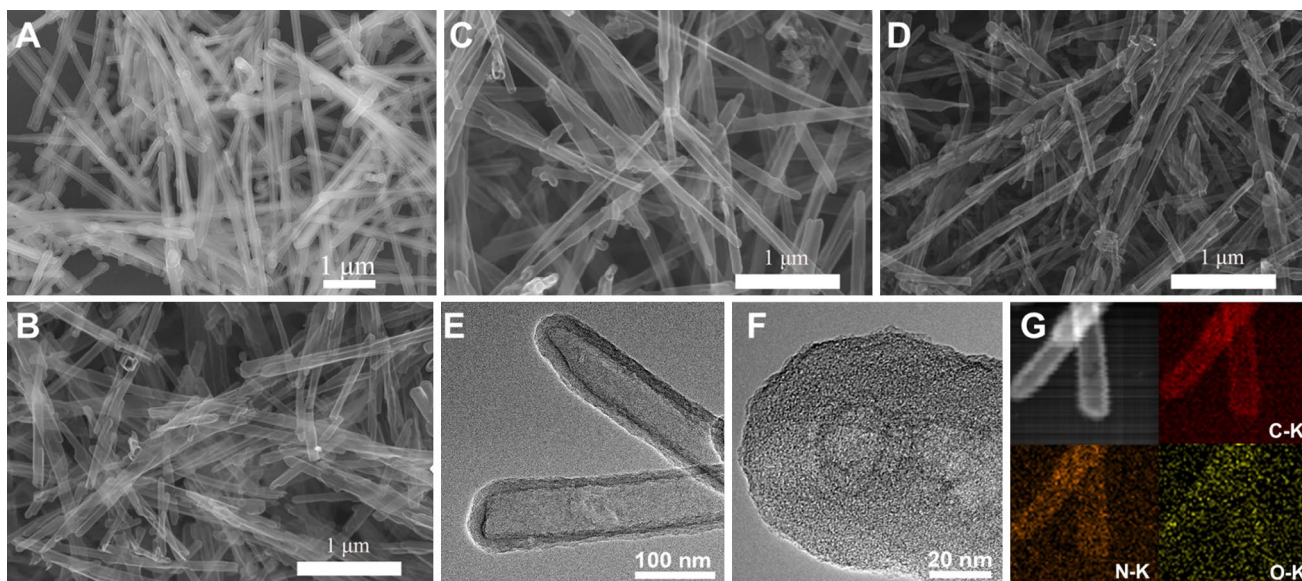


Fig. 1 Representative SEM images of ZnO@PDA (a), NCNT-800 (b), NCNT-900 (c), NCNT-1000 (d), TEM images of NCNT-900 (e and f) and elemental mapping images of NCNT-900 (g)

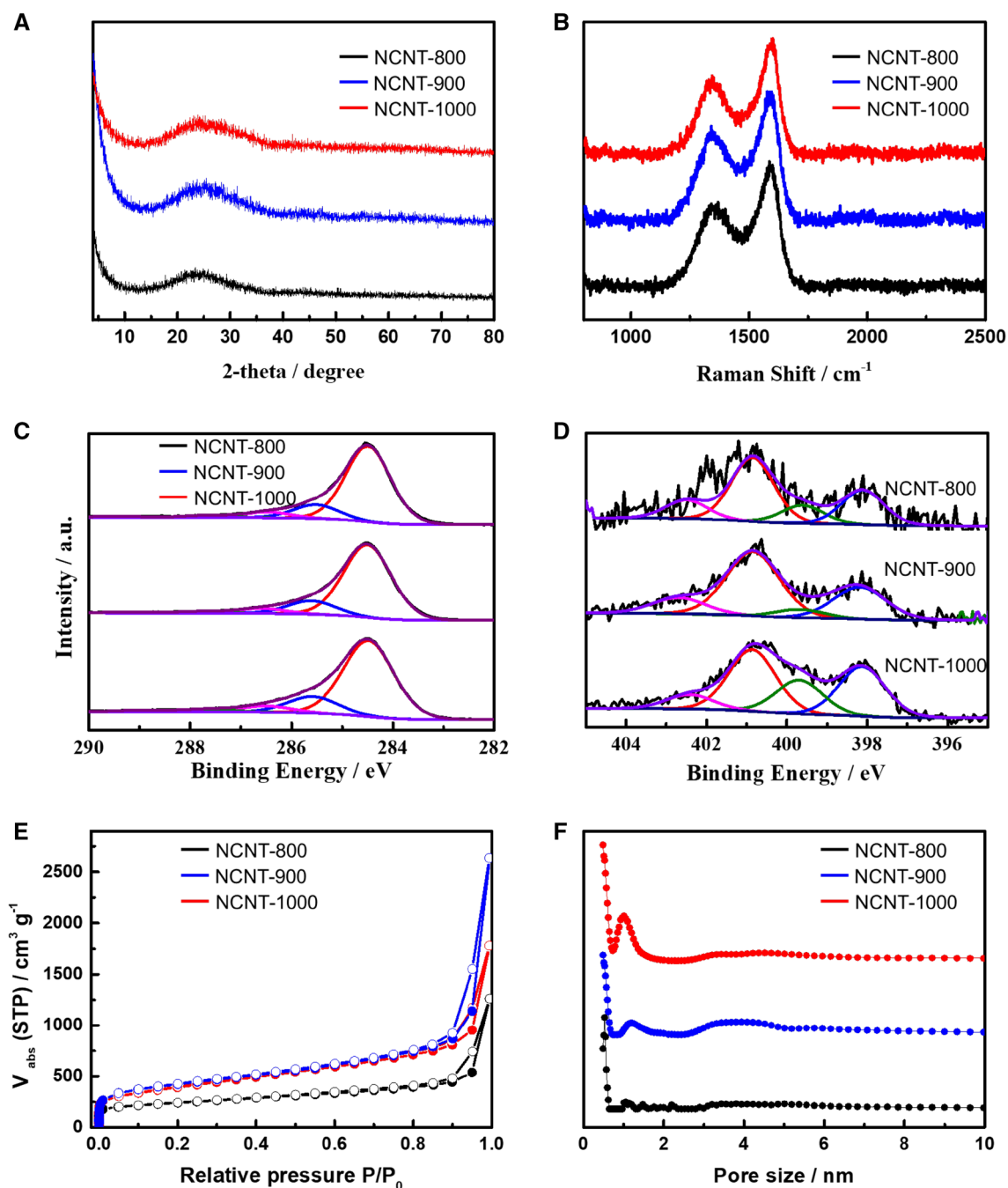


Fig. 2 **a** XRD patterns of NCNT-800, NCNT-900 and NCNT-1000. **b** Raman spectra of NCNT-800, NCNT-900 and NCNT-1000. **c** High-resolution C 1 s core-level XPS spectra of NCNT-800, NCNT-900 and NCNT-1000. **d** High-resolution N 1 s core-level XPS spectra of

NCNT-800, NCNT-900 and NCNT-1000. **e** N₂ adsorption/desorption isotherms of NCNT-800, NCNT-900 and NCNT-1000. **f** The pore-size distribution curves calculated from the adsorption branch of the isotherms by the QSDFT method

graphitic N (400.9 eV), and oxidized N (402.6 eV) (Fig. 2d) [36–38]. Pyridinic N and graphitic N are generally considered as highly efficient active species for ORR; thus, we calculated the Pyridinic N and graphitic N content of the catalyst according to their integral area ratio of the total N content. For NCNT-800, NSNT-900 and NCNT-1000, the

Pyridinic N and graphitic N account for 78%, 84% and 63% of the total N content. It should be noted that the active N content of up to 84% for NCNT-900 makes it very competitive as an ORR catalyst.

Porosity, especially surface area is another very important factor that affects the catalytic activity of catalysts. Nitrogen

adsorption measurements were conducted to investigate the specific surface area and porous structure of the catalysts (Fig. 2e). All the samples show type-I isotherms with a sharp increase in the low-pressure range, indicating plenty of micropores exist in the catalysts. The Brunauer-Emmett-Teller (BET) surface areas are 850, 1312 and 1298 $\text{m}^2 \text{g}^{-1}$ for NCNT-800, NCNT-900 and NCNT-1000. Obviously, NCNT-900 and NCNT-1000 exhibit a much higher surface area than NCNT-800. This can be ascribed to the evaporation of Zn at high temperatures above 900 °C. The evaporation of Zn should pass through the nanotube, which will leave many voids in the carbon, thus leading to high surface area. Pore-size distribution (PSD) analysis shows that the pores of the catalysts are mostly located at 0.6 and 1.1 nm, in accordance with the results from the adsorption isotherms (Fig. 2f). Though no obvious mesopores can be observed,

the tubular can be expected to facilitate mass transport during the catalysis process. Thus, the catalytic activity of the catalysts is expected to be very attractive.

3.2 ORR Performance of the Catalysts

The ORR performance of the catalysts was first evaluated by cyclic voltammetry (CV) in 0.1 M KOH solution. As shown in Fig. 3a, no redox peak can be observed in N_2 -saturated electrolyte, while an obvious O_2 reduction peak appeared in O_2 -saturated electrolyte, suggesting that the catalysts can catalyze the ORR. Moreover, the cathodic peak position of NCNT-900 and NCNT-1000 is more positive than that of NCNT-800, demonstrating their superiority. Linear scanning voltammetry (LSV) curves also demonstrated the same result. As shown in Fig. 3b, the onset potentials for

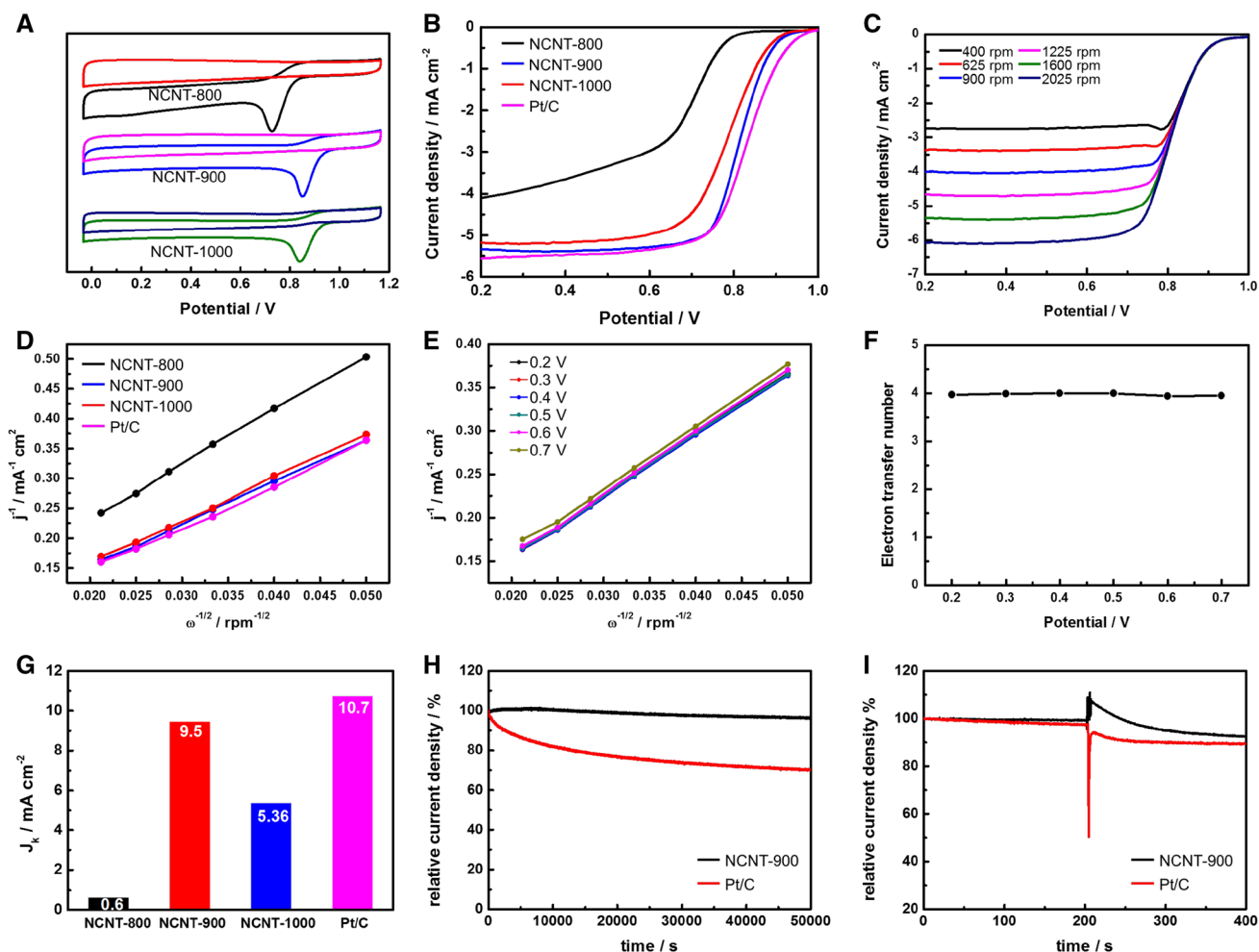


Fig. 3 a CV curves of NCNT-800, NCNT-900 and NCNT-1000 measured in an O_2 and N_2 saturated 0.1 M KOH solution. b RDE polarization curves of Pt/C, NCNT-800, NCNT-900 and NCNT-1000. c RDE polarization curves of NCNT-900 at different rotating speed. d K-L plots of Pt/C, NCNT-800, NCNT-900 and NCNT-1000 at 0.5 V. e K-L plots of NCNT-900 at different potentials. f The electron trans-

fer number of NCNT-900. g The kinetic current density of NCNT-800, NCNT-900 and NCNT-1000 at 0.8 V. h Chronoamperometric curves of NCNT-900 and Pt/C in O_2 -saturated 0.1 M KOH solution at a rotation rate of 1600 rpm for 50,000 s at 0.4 V. i Chronoamperometric response for of NCNT-900 and Pt/C electrodes on addition of 20 mL methanol to 180 mL of electrolyte

NCNT-800, NCNT-900 and NCNT-1000 are 0.849, 0.955 and 0.952 V respectively, indicating that the ORR takes place earlier on NCNT-900. Moreover, the half wave potentials also follow the same trend, with values of NCNT-900 (0.815 V) > NCNT-1000 (0.791 V) > NCNT-800 (0.662 V). The superior properties of NCNT-900 and NCNT-1000 compared with NCNT-800 can be ascribed to their higher surface area, demonstrating the importance of the surface areas for ORR. For NCNT-900 and NCNT-1000, which possess similar surface area and structure, the better property of NCNT-900 can be ascribed to its higher N content, highlighting the important role of heteroatom doping. Thus, for ORR catalysts, high surface and heteroatom content are both very important factors for realizing increased catalytic activity. Though the ORR performance for NCNT-900 is still weaker than that for 20 wt% Pt/C in terms of the onset and half wave potential, the limiting current density for NCNT-900 is almost comparable with that obtained for Pt/C catalysts. Considering its much lower price and facile preparation method, NCNT-900 is still very attractive.

To gain further insight into the ORR kinetics and mechanisms, LSV polarization curves were recorded at various rotation rates. As shown in Fig. 3c and S6, the diffusion current densities increased with increasing rotating rates due to a shortened diffusion distance at high rotating speeds. The Koutecky-Levich (K-L) plots exhibit a linear relationship between j^{-1} and $\omega^{-1/2}$, indicating that there is a positive correlation between the reaction rates and the concentration of dissolved O_2 [39]. From the slopes of the K-L plots, the electron transfer number was calculated. The electron transfer number is 3.07 for NCNT-800 at 0.4 V, indicating that both the 2-electron pathway and 4-electron pathway takes place in it. However, for NCNT-900 and NCNT-1000, the electron transfer numbers are all close to four (4.00 for NCNT-900, 3.92 for NCNT-1000 and 3.98 for Pt/C), suggesting that the ORR undergoes a direct four electron pathway. The K-L curves were calculated at various potentials from 0.2 to 0.7 V, and it can be seen that the electron transfer numbers are all close to four, once again highlighting the effectiveness of NCNT-900 (Fig. 3e, f). The kinetic current density (J_k), an inherent measure of the intrinsic activity of the catalyst, was calculated from the intercept of the K-L curve [40]. The value of J_k for NCNT-900 (9.5 mA cm^{-2}) is also larger than that for NCNT-800 (0.6 mA cm^{-2}) and NCNT-1000 (5.4 mA cm^{-2}) at 0.8 V, and comparable to that obtained for commercial Pt/C (10.7 mA cm^{-2}) (Fig. 3g). Obviously, the NCNT-900 exhibits a superior ORR performance in terms of the onset and half wave potential, electron transfer number and kinetic limiting current density. For the three samples, NCNT-900 shows the best catalytic activity due to its structure and composition. Compared with NCNT-800, NCNT-900 has a larger surface area, which can provide more exposed active sites and faster mass transport. Thus,

the catalytic activity of NCNT-900 is increased. Compared with NCNT-1000, whose surface area is also very high. NCNT-900 has a higher N content, which is very important for providing active sites. Therefore, the high surface area and high N doping contributed to the high performance of NCNT-900.

For the practical application of ORR catalysts, long-term durability is also very crucial. The durability of the NCNT-900 was measured by chronoamperometric at 0.3 V and 1600 rpm. 90% of the current density of NCNT-900 was maintained after testing for 50,000 s, while this value is only 70% for the Pt/C catalyst. This can be explained by the composition of NCNT-900. As there is no metal in the catalyst, no aggregation issues exist in it. Moreover, the carbon nanotube is usually rigid, and it possesses high physical and chemical stability. In addition to the excellent durability, NCNT-900 also displays good methanol tolerance, which overcomes another disadvantage faced by the Pt/C catalyst. When 20 ml methanol was injected into 180 ml electrolyte, the Pt/C catalyst exhibited a large current decrease due to methanol poisoning, while the NCNT-900 remains almost unaffected by methanol, indicating that it can be used for a directed methanol fuel cell (Fig. 3i).

3.3 HER Performance of the Catalysts

In addition to the high ORR performance, the NCNTs also exhibit excellent HER activity. As shown in Fig. 4a, the HER performance of the catalysts was investigated in 1.0 M KOH. Obviously, NCNT-900 shows a much lower onset potential, with polarization current increasing more rapidly, indicating its higher activity. The current density of 10 mA cm^{-2} is a critical metric in solar fuel production; thus, the overpotential at 10 mA cm^{-2} was compared. These values are 500, 350 and 450 mV for NCNT-800, NCNT-900 and NCNT-1000 respectively, indicating that NCNT-900 can be used to save more energy when an equal amount of H_2 is produced from water. Tafel slopes were used to explore the HER mechanism. The Tafel slope is 132 mV dec^{-1} for NCNT-900, suggesting that the HER over NCNT-900 proceeded via a Volmer-Heyrovsky mechanism, with an initial proton adsorption being the rate-determining step (Fig. 4b) [41, 42]. Moreover, the Tafel slope for NCNT-900 is also lower than that for NCNT-800 (177 mV dec^{-1}), demonstrating faster HER kinetics for NCNT-900. Moreover, the HER performance of NCNT-900 is still higher than those of $C_3N_4@NG$, [43] N, S-CN, [23] ONPPGC/OCC, [44] NG [45] and comparable with that of NWCNT [19]. The double layer capacitances (C_{dl}), which is proportional to the electrochemically active surface area (ECSA) of the catalysts, was measured by the CV method at different scan rates (Fig. 4d, e and S7). Obviously, the C_{dl} for NCNT-900 was found to be 51 mF cm^{-2} , which is larger than that obtained for NCNT-800 (38

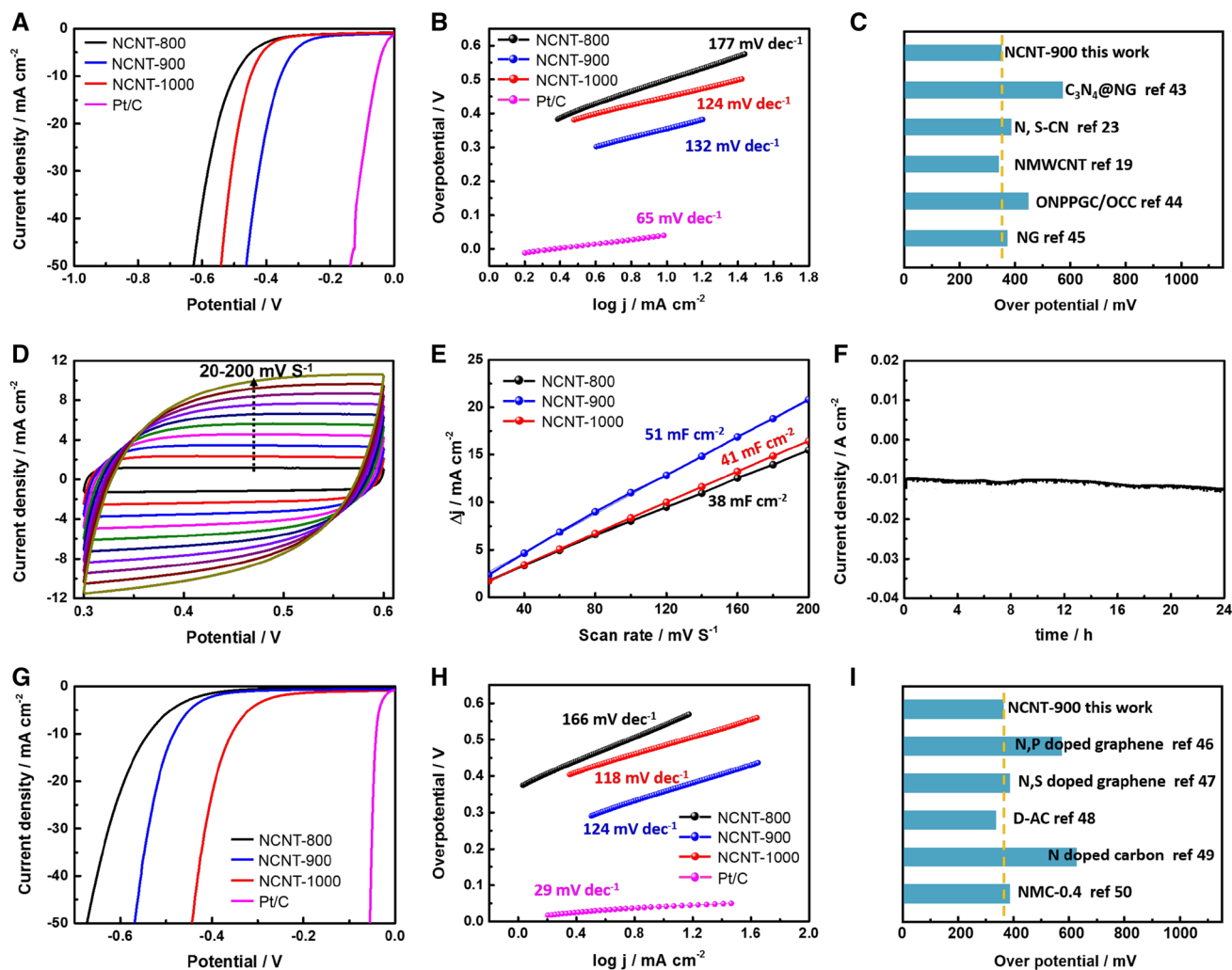


Fig. 4 **a** HER polarization curves of Pt/C, NCNT-800, NCNT-900 and NCNT-1000 in 1.0 M KOH. **b** Tafel slopes of Pt/C, NCNT-800, NCNT-900 and NCNT-1000 in 1.0 M KOH. **c** HER overpotentials of typical carbon catalysts at 10 mA cm^{-2} in 1.0 M KOH. **d** CV curves of NCNT-900 at different scan rates. **e** The capacitive current densities at 0.45 V as a function of the scan rate for NCNT-800, NCNT-

900 and NCNT-1000. **f** Chronoamperometric response of NCNT-900 at a constant potential of 350 mV for 24 h. **g** HER polarization curves of Pt/C, NCNT-800, NCNT-900 and NCNT-1000 in 0.5 M H_2SO_4 . **h** Tafel slopes of Pt/C, NCNT-800, NCNT-900 and NCNT-1000 in 0.5 M H_2SO_4 . **i** HER overpotentials of typical carbon catalysts at 10 mA cm^{-2} in 0.5 M H_2SO_4

mF cm^{-2}) and NCNT-1000 (41 mF cm^{-2}), indicating that NCNT-900 is more effective in enlarging the catalytic surface area, and correspondingly, provides more active sites. Moreover, NCNT-900 also exhibits good durability. Using the chronoamperometry method at a constant overpotential of 350 mV, the current density shows almost no change for 24 h. Such performances can be rationalized in terms of the nanotube structure, which facilitates gas detachment, and the high stability of the carbon nanotube.

Motivated by the above HER activity in 1.0 M KOH, we also explored the HER performance of the NCNTs in 0.5 M H_2SO_4 . Similarly, the catalytic activity follows the same trend as that found in the alkaline medium (Fig. 4g).

To achieve a current density of 10 mA cm^{-2} , NCNT-900 requires an overpotential of 360 mV, which is lower than that for NCNT-800 (540 mV) and NCNT-1000 (480 mV). Additionally, NCNT-900 exhibits the lowest Tafel slope of 124 mV dec^{-1} , indicating that the Volmer-Heyrovsky mechanism is the principal HER mechanism (Fig. 4h). It should be noted that the HER activity of NCNT-900 is higher or comparable with those of recently reported carbon-based catalysts such as N, S co-doped graphene [46], N, P co-doped graphene [47], D-AC [48], N doped carbon [49], N doped mesoporous carbon (NMC-0.4), [50] etc., making it one of the most active carbon-based catalysts for the HER (Fig. 4i).

4 Conclusions

In conclusion, taking advantage of the ZnO template, we have developed a facile strategy to synthesis N doped carbon nanotubes as highly efficient ORR and HER catalysts. The optimized NCNT-900 shows high ORR performance comparable with that obtained for Pt/C and a good HER performance in both alkaline and acid media. The high performance can be attributed to a high surface area and unique textural parameters, which lead to enhanced mass transfer properties, and effective N doping that provides an abundance of active sites. It is anticipated that the activity of the carbon nanotube obtained using this strategy can be further improved by rational design of the carbon precursor with higher N content or multi-heteroatom co-doping.

Acknowledgements This work is supported financially by the National Natural Science Foundation of China (Grant No. 51772039), the Fundamental Research Funds for the Central University (DUT18LK13) and the Research Center for Solar Light Energy Conversion, Kyushu Institute of Technology, Japan.

Compliance with Ethical Standards

Conflict of interest The authors declare no conflict of interest.

References

- Cook TR, Dogutan DK, Reece SY, Surendranath Y, Teets TS, Nocera DG (2010) *Chem Rev* 110:6474
- Turner JA (2004) *Science* 305:972
- Lewis NS, Nocera DG (2006) *Proc Natl Acad Sci USA* 103:15729
- Duan J, Chen S, Jaroniec M, Qiao S (2015) *ACS Catal* 5:5207
- Wang J, Xu F, Jin H, Chen Y, Wang Y (2017) *Adv Mater* 29:1605838
- Huang Z, Wang J, Peng Y, Jung C, Fisher A, Wang X (2017) *Adv Energy Mater* 7:1700544
- Li J, Hou P, Liu C (2017) *Small* 7:1702002
- Debe MK (2012) *Nature* 486:43
- Cheng N, Banis MN, Liu J, Riese A, Mu S, Li R, Sham TK, Sun X (2015) *Energy Environ Sci* 8:1450
- Wu G, Zelenay P (2013) *Acc Chem Res* 46:1878
- Fan X, Zhou H, Guo X (2015) *ACS Nano* 9:5125
- Jin Y, Wang H, Li J, Yue X, Han Y, Shen PK, Cui Y (2016) *Adv Mater* 28:3785
- Li Y, Xu H, Huang H, Gao L, Zhao Y, Ma T (2017) *Electrochim Acta* 254:148
- Li JC, Hou PX, Zhang L, Liu C, Cheng HM (2014) *Nanoscale* 6:12065
- Liu X, Zhou W, Yang L, Li L, Zhang Z, Ke Y, Chen S (2015) *J Mater Chem A* 3:8840
- Gong K, Du F, Xia Z, Durstock M, Dai L (2009) *Science* 323:760
- Zhao Y, Yang L, Chen S, Wang X, Ma Y, Wu Q, Jiang Y, Qian W, Hu Z (2013) *J Am Chem Soc* 135:1201
- Guo D, Shibuya R, Akiba C, Saji S, Kondo T, Nakamura J (2016) *Science* 351:361
- Davodi F, Tavakkoli M, Lahtinen J, Kallio T (2017) *J Catal* 353:19
- Wang D, Su D (2014) *Energy Environ Sci* 7:576
- Paraknowitsch JP, Thomas A (2013) *Energy Environ Sci* 6:2839
- Gong YJ, Fei HL, Zou XL, Zhou W, Yang SB, Ye GL, Liu Z, Peng ZW, Lou J, Vajtai R, Yakobson BI, Tour JM, Ajayan PM (2015) *Chem Mater* 27:1181
- Qu K, Zheng Y, Zhang X, Davey K, Dai S, Qiao S (2017) *ACS Nano* 11:7293
- Song Z, Liu W, Cheng N, Banis MN, Li X, Sun Q, Xiao B, Liu Y, Lushington A, Li R, Liu L, Sun X (2017) *Mater Horiz* 4:900
- Chen Y, Wang C, Wu Z, Xiong Y, Xu Q, Yu S, Jiang H (2015) *Adv Mater* 27:5010
- Ferrero GA, Preuss K, Fuertes AB, Sevilla M, Titirici MM (2016) *J Mater Chem A* 4:2581
- Xing T, Zheng Y, Li L, Cowie BCC, Gunzelmann D, Qiao S, Huang S, Chen Y (2014) *ACS Nano* 8:6856
- Liu R, Wu D, Feng X, Mullen K (2010) *Angew Chem* 122:2619
- Ding W, Wei Z, Chen S, Qi X, Yang T, Hu J, Wang D, Wan L, Alvi S, Li L (2013) *Angew Chem Int Ed* 52:11755
- Shuai XM, Shen WZ WZ (2011) *J Phys Chem C* 2011, 115:6415
- Zhang Z, Yi Z, Wang J, Tian X, Xu P, Shi G, Wang S (2017) *J Mater Chem A* 5:17064
- Chen B, Li F, Mei Q, Yang Y, Liu H, Yuan G, Han B (2017) *Chem Commun* 53:13019
- Li Y, Xu H, Huang H, Gao L, Ma T (2018) *J Electrochem Soc* 165:F158
- Cheon JY, Kim JH, Kim J, Goddeti JH, Park KC, Joo JY SH (2014) *J Am Chem Soc* 136:8875
- Ding W, Li L, Xiong K, Wang Y, Li W, Nie Y, Chen S, Qi X, Wei Z (2015) *J Am Chem Soc* 137:5414
- Fechler N, Zussblatt NP, Rothe R, Schlogl R, Willinger MG, Chmelka BF, Antonietti M (2016) *Adv Mater* 28:1287
- Li S, Cheng C, Liang H, Feng X, Thomas A (2017) *Adv Mater* 29:1700707
- Wei W, Liang H, Parvez K, Zhuang X, Feng X, Mullen K (2014) *Angew Chem Int Ed* 53:1570
- Muthukrishnan A, Nabae Y, Chang C, Okajimaa T, Ohsaka T (2015) *Catal Sci Technol* 5:1764
- Singh D, Jenjeti R, Sampath S, Eswaramoorthy M (2017) *J Mater Chem A* 5:6025
- Skulason E, Tripkovic V, Bjorketun ME, Gudmundsdottir S, Karlberg G, Rossmeisl J, Bligaard T, Jonsson H, Norskov JK (2010) *J Phys Chem C* 114:18182
- Conway BE, Tilak BV (2002) *Electrochim Acta* 47:3571
- Zheng Y, Jiao Y, Zhu Y, Li H, Han L, Chen Y, Du Y, Jaroniec A, Qiao M S (2014) *Nat Commun* 5:3783
- Lai J, Li S, Wu F, Saqi M, Luque R, Xu G (2016) *Energy Environ Sci* 9:1210
- Yue X, Huang S, Cai J, Jin Y, Shen P (2017) *J Mater Chem A* 5:7784
- Zheng Y, Jiao Y, Li L, Xing T, Chen Y, Jaroniec M, Qiao S (2014) *ACS Nano* 8:5290
- Ito Y, Cong W, Fujita T, Tang Z, Chen M (2015) *Angew Chem Int Ed* 54:2131
- Yan X, Jia Y, Odedairo T, Zhao X, Jin Z, Zhu Z, Yao X (2016) *Chem Commun* 52:8156
- Zhang B, Wen Z, Ci S, Chen J, He Z (2014) *RSC Adv* 4:49161
- Zhao X, Li S, Cheng H, Schmidt J, Thomas A (2018) *ACS Appl Mater Interfaces* 10:3912

Affiliations

Yanqiang Li¹ · Huiyong Huang¹ · Siru Chen³ · Chao Wang¹ · Anmin Liu¹ · Tingli Ma²

✉ Yanqiang Li
yanqiangli@dlut.edu.cn

✉ Siru Chen
chen2766348@126.com

✉ Tingli Ma
tinglima@dlut.edu.cn

² Graduate School of Life Science and Systems Engineering, Kyushu Institute of Technology, 2-4 Hibikino, Wakamatsu, Kitakyushu, Fukuoka 808-0196, Japan

³ State Key Laboratory of Catalysis, iChEM, Dalian Institute of Chemical Physics, the Chinese Academy of Sciences, Dalian 116023, China

¹ State Key Laboratory of Fine Chemicals, School of Petroleum and Chemical Engineering, Dalian University of Technology, Panjin Campus, Panjin 124221, China